Molecular Microbiology (2010) 76(4), 833–847 ■
doi:10.1111/j.1365-2958.2010.07153.x
First published online 22 April 2010

Membrane invagination in *Rhodobacter sphaeroides* is initiated at curved regions of the cytoplasmic membrane, then forms both budded and fully detached spherical vesicles

Jaimey D. Tucker,[1] C. Alistair Siebert,[2†] Maryana Escalante,[3] Peter G. Adams,[1] John D. Olsen,[1] Cees Otto,[3] David L. Stokes[2,4] and C. Neil Hunter[1]*

[1]*Department of Molecular Biology and Biotechnology, University of Sheffield, Western Bank, Firth Court, Sheffield S10 2TN, UK.*
[2]*The New York Structural Biology Centre, 89 Convent Avenue, New York, NY 10027, USA.*
[3]*Biophysical Engineering Group, MESA+ Institute for Nanotechnology, University of Twente P.O. Box 217, 7500 AE Enschede, the Netherlands.*
[4]*Skirball Institute of Biomolecular Medicine, School of Medicine, New York University, 540 First Avenue, New York, NY 10016, USA.*

Summary

The purple phototrophic bacteria synthesize an extensive system of intracytoplasmic membranes (ICM) in order to increase the surface area for absorbing and utilizing solar energy. *Rhodobacter sphaeroides* cells contain curved membrane invaginations. In order to study the biogenesis of ICM in this bacterium mature (ICM) and precursor (upper pigmented band – UPB) membranes were purified and compared at the single membrane level using electron, atomic force and fluorescence microscopy, revealing fundamental differences in their morphology, protein organization and function. Cryo-electron tomography demonstrates the complexity of the ICM of *Rba. sphaeroides*. Some ICM vesicles have no connection with other structures, others are found nearer to the cytoplasmic membrane (CM), often forming interconnected structures that retain a connection to the CM, and possibly having access to the periplasmic space. Near-spherical single invaginations are also observed, still attached to the CM by a 'neck'. Small indents of the CM are also seen, which are proposed to give rise to the UPB precursor membranes upon cell disruption. 'Free-living' ICM vesicles, which possess all the machinery for converting light energy into ATP, can be regarded as bacterial membrane organelles.

Accepted 22 March, 2010. *For correspondence. E-mail c.n.hunter@sheffield.ac.uk; Tel. (+44) 114 222 4191; Fax (+44) 114 222 2711. †Present address: Division of Structural Biology, University of Oxford, Oxford OX3 7B, UK.

Introduction

All cells require a source of energy, usually provided by membrane–protein complexes housed by the internal membranes within an organelle. Some bacteria also contain intracytoplasmic membranes (ICM), which in some cases resemble the elaborations of membranes found in mitochondria and chloroplasts (Niederman, 2006). The morphology of such energy-yielding membranes is driven by the requirement to increase the membrane surface area for the membrane-bound enzymes that mediate electron and proton transfers. In the case of photosynthetic prokaryotes, which form part of the phytoplankton that carry out a significant proportion of global photosynthesis (Field *et al.*, 1998), there is an additional requirement arising from the scarcity of light, especially deep in the oceans, which demands that the surface area for light absorption is greatly increased. Oceanic cyanobacteria such as *Prochlorococcus*, which grow to depths of over 100 m (Johnson *et al.*, 2006), contain up to five tightly appressed, concentric layers of ICM, which house the light-gathering chlorophyll–protein complexes. Cryo-electron tomography of *Prochlorococcus* cells shows that these internal membranes are interconnected (Ting *et al.*, 2007), similar to the highly connected membrane networks observed in two other cyanobacterial species, *Synechococcus elongatus* PCC 7942 and *Microcoleus* sp. (Nevo *et al.*, 2007).

Given the functional importance of the internal membranes of photosynthetic bacteria it is important to understand the inception of membrane growth. The ICM of the purple phototrophic bacterium *Rhodobacter sphaeroides* provide a well-characterized system for studying membrane biogenesis. The organization and connectivity of

chlorophyll–protein complexes in the native ICM of *Rba. sphaeroides* has been mapped to high resolution by tapping mode atomic force microscopy (AFM) (Bahatyrova *et al*., 2004a), and has also been probed extensively by spectroscopic methods (Hunter *et al*., 1985; Vos *et al*., 1988; Frese *et al*., 2000; 2004). Finally, a combination of AFM, cryo-electron microscopy (cryo-EM), nuclear magnetic resonance (NMR) and spectroscopic approaches has been used to construct an atomic model of a single ICM vesicle, consisting of approximately 150 membrane protein complexes (Sener *et al*., 2007). The sites of initiation of membrane budding and vesicle formation were discovered by Niederman and co-workers, who isolated an upper pigmented band (UPB) which sediments through sucrose-density gradients more slowly than ICM vesicles during rate-zone centrifugation. They used pulse-chase radiolabelling to demonstrate a direct precursor–product relationship between the UPB and ICM fractions, suggesting that the UPB membranes contain sites of initiation of membrane invagination, derived from the cytoplasmic membrane (CM), which is closely appressed to the cell wall (Niederman *et al*., 1979; Inamine *et al*., 1984; Reilly and Niederman, 1986). The biosynthetic role of these UPB membranes was also established by a series of functional studies (Hunter *et al*., 1979a,b; Bowyer *et al*., 1985; Koblizek *et al*., 2005).

Here, cryo-electron tomography has been used to investigate the three-dimensional (3-D) internal membrane structure of *Rba. sphaeroides* cells. We have identified several classes of ICM, a number of which have budded off and separated completely from their point of origin at the CM and exist as a true bacterial organelle, a vesicle of approximately 50 nm in diameter that can carry out the core function of the cell, namely the conversion of solar energy into ATP. The curved sites of initiation of membrane budding, clearly defined *in situ* by the tomographic analysis and also purified from UPB fractions, retain their curvature following purification and analysis by transmission electron microscopy (TEM). AFM has revealed the organization of the protein complexes within these membrane initiation sites; confocal microscopy and spectral analysis of the fluorescence emission from single-membrane fragments shows that there is a lesion in the functional associations of LH complexes embedded in the precursor membrane.

Results

Pulse-chase analysis confirms a precursor–product relationship between UPB and ICM structures in Rba. sphaeroides

Disruption of photosynthetically grown *Rba. sphaeroides* cells in a French press, followed by rate-zonal centrifugation on sucrose gradients, yields two pigmented membrane fractions (Fig. 1A). Pulse-chase radiolabelling with [S^{35}] methionine was carried out in order to align our experiments with earlier studies which demonstrated that the upper and lower membrane bands have a biosynthetic relationship, and originate from immature and mature membranes respectively (Niederman *et al*., 1979; Inamine *et al*., 1984; Reilly and Niederman, 1986). Figure 1B shows that a short pulse of radiolabel is incorporated almost instantaneously into the UPB membrane, with a subsequent decline over the 250 min time-course of the chase with unlabelled methionine. In contrast, a significantly lower level of radiolabel is incorporated into the ICM fraction and the extent of labelling rises during the chase. Thus, we observe a precursor–product relationship between the UPB and ICM fractions (Fig. 1B). When a protein synthesis inhibitor (chloramphenicol) is added along with the chase, the [S^{35}] methionine label persists in the UPB fraction (Fig. 1B, black dotted line). Therefore, ongoing protein synthesis is required to convert these UPB sites of incorporation of radiolabel to a more invaginated ICM structure. These results are in agreement with previous studies (Niederman *et al*., 1979; Inamine *et al*., 1984; Reilly and Niederman, 1986) and demonstrate that

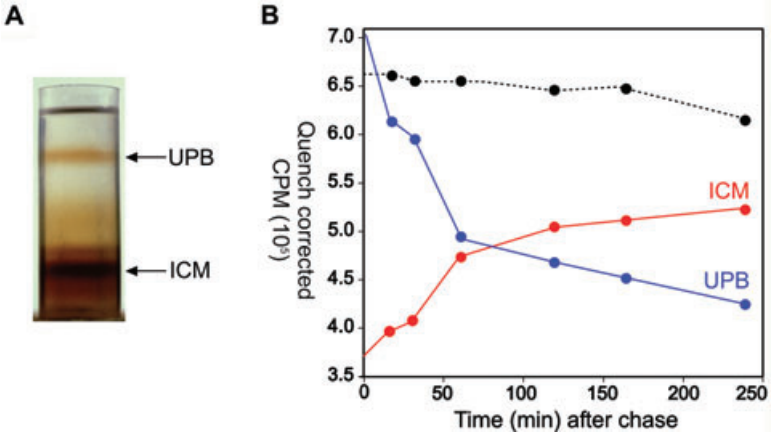

Fig. 1. Rate-zone ultracentrifugation characteristics of a cell extract from *Rba. sphaeroides* and pulse-chase activity of isolated membrane fractions.
A. Separation into ICM and UPB membrane fractions by rate-zone ultracentrifugation on a 5–35% w/w sucrose gradient, following cell disruption.
B. Pulse-chase labelling characteristics of isolated membrane fractions using S^{35}-labelled methionine. After addition of the chase with unlabelled methionine at time zero, the level of radiolabel in the UPB fraction decreases (blue line), concomitant with the increase in ICM radiolabelling (red line). In a chloramphenicol-treated culture the level of radiolabel in the UPB fraction remains relatively constant (black dotted line).

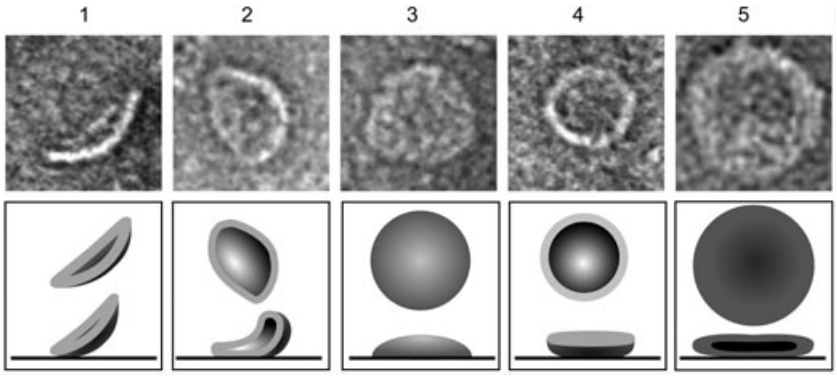

Fig. 2. Transmission electron microscopy of isolated ICM and UPB membranes. The upper row depicts five electron micrographs of typical images of the UPB (1–4) and ICM (5). The white features are likely to be the protein-rich lipid bilayer viewed nearly edge-on. The lower row shows cartoon interpretations of the EM images where the upper cartoon corresponds to the observed shape of the isolated membrane and the lower one is a hypothetical interpretation of the shape viewed along the plane of the grid. All boxes represent a 100 × 100 nm square from each EM image.

the UPB membrane, used for the present structural and functional work, is derived from sites of ICM assembly where budding of the CM is initiated.

The precursor and mature membranes retain distinct morphologies in the purified state

It is not immediately obvious why the mature and the precursor membranes form distinct membrane bands upon rate-zone sedimentation through sucrose gradients, a fortuitous separation which is an essential first step in identifying the biosynthetic relationship between these membrane fractions. TEM was used to identify any morphological differences between the membranes in the upper and lower bands that could form the basis for this separation in sucrose density gradients. First, contaminating CM, ribosomes and loosely associated proteins were removed from the UPB sucrose gradient fraction using a further round of sucrose gradient ultracentrifugation. The physical shapes of the purified membranes were analysed using TEM, and then AFM was used to determine the arrangements of photosynthetic complexes within isolated individual UPB and intracytoplasmic membranes.

Transmission electron microscopy of purified, negatively stained UPB membranes yielded a variety of images; an example of each class of projection is shown in Fig. 2 columns 1–4. More images are displayed in Fig. S1 in *Supporting information*. Images 1 and 2 represent side-on or partially side-on projections, which show an open, hollow, hemispherical membrane structure with a convex external surface; such images are never observed in the ICM fraction. Figure 2 columns 3 and 4 show the convex upper surface and concave inner surface of the UPB membranes respectively. This view also confirms the hollow hemispherical nature of the UPB membranes, which allows pooling of stain in the centre and leads to high contrast with the relatively poorly staining rim. Some heterogeneity in the size of this precursor membrane is apparent in these images. Figure 2 column 5 shows a representative projection of a flattened ICM vesicle which differs from UPB membranes in two significant ways: first, only one class of projection is largely seen, suggesting that these negatively stained membranes originate from a closed spherical structure, approximately 50 nm diameter, and, second, ICM vesicles have a more homogenous size, in marked contrast with the more variable UPB membrane. The ~100 nm diameter of the flattened structure in Fig. 2 column 5 strongly suggests that the 50 nm-diameter vesicles collapse during the desiccation process prior to EM imaging, leading to a flattened ovoid shape; see the cartoon representation in Fig. 2 column 5. We suggest that the contrasting morphologies of UPB membranes and ICM vesicles give rise to the separation into two distinct bands during rate-zone sedimentation, and that this difference reflects their varying cellular origin, with the UPB membranes breaking away from their CM anchoring points during French press treatment, and a substantial proportion of the ICM vesicles being liberated from the cytoplasm in their native spherical state. Another portion of the ICM vesicles would be expected to arise from the membrane continuum which, when disrupted, fractures at connecting vesicle necks into structures indistinguishable from those that have naturally budded off, as confirmed by the observed uniformity of ICM vesicle sizes.

Identification of light-harvesting LH2 and RC-LH1-PufX complexes in AFM topographs of single UPB and ICM

In order to investigate the protein organization of these two types of purified membrane further, AFM was used to image the topology of membranes adsorbed onto a mica support under liquid, at near-native conditions of pH, temperature and ionic strength. We found that UPB membranes adsorb poorly onto the mica substrate, possibly because only the rim of the curved membrane patch makes contact with the surface. This poor adhesion leads to a tendency of the membrane to move during imaging, which necessitates the use of very gentle tapping mode AFM. In the case of ICM, treatment with very low concentrations of detergent [0.01% (w/v) β-dodecyl maltoside] was required to open the vesicles so that patches

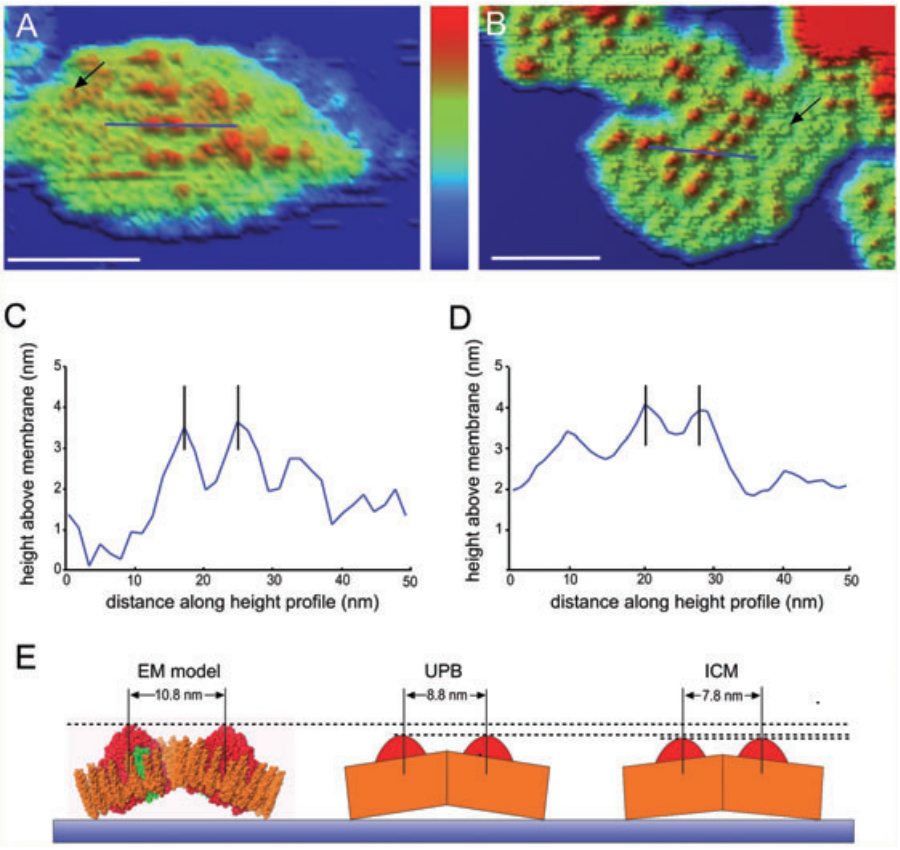

Fig. 3. Atomic force microscopy of individual UPB and intracytoplasmic membranes.
A and B. Three-dimensionally rendered AFM height images of (A) a UPB membrane and (B) an ICM patch, each adsorbed to a mica surface. In each panel, a black arrow indicates a light-harvesting LH2 complex. Each blue line represents a 50-nm-height profile across the surface of the membrane, centred upon a dimeric RC-LH1-PufX complex. The height data are displayed in (C) and (D) respectively. (A) and (B) are segments from data collected at 512 × 512 pixels. The full *z* range, as depicted by the blue to red spectrum bar, is 11 nm for (A) and 7 nm for (B) and the scale bars are 50 nm.
C and D. Height profiles of a single dimeric RC-LH1-PufX complex, in (C) a UPB and (D) an ICM patch. It should be noted that the heights are relative to the surface of the membrane in each case and not to the underlying mica substrate. The average centre-to-centre separation of the highest point of the RC-H subunits is 8.8 ± 0.7 nm ($n = 9$) for the UPB patch in (A) and 7.8 ± 1.1 nm ($n = 24$) for the ICM patch in (B).
E. Diagram showing the structure of the core dimer complex from data in Qian *et al.* (2005; 2008) (left) alongside a schematic of the same complex; the effect of a slight flattening of the complex is to lower its height above the mica surface, as well as to shorten the separation between the highest points of the RC-H subunits. This effect is seen in both membranes, but is more marked in the case of the ICM patches (right), than in the UPB patch (middle).

consisting of one membrane bilayer can adsorb and flatten onto the mica support.

Medium-resolution AFM topographs of the UPB and intracytoplasmic membranes are displayed in Fig. 3A and B. A 3-D representation of the cytoplasmic surface of an individual UPB membrane adsorbed onto mica is compared with a patch from an ICM vesicle. The full *z* range in each image, depicted by the blue-to-red bar, is 11 nm in Fig. 3A and 7 nm in Fig. 3B. The most strongly protruding structures, in red, are dimeric proteins, and the other major protein molecules in each membrane are circular complexes approximately 8 nm in diameter with typical examples highlighted with black arrows. By analogy with earlier AFM work on *Rba. sphaeroides* membranes (Bahatyrova *et al.*, 2004a; Olsen *et al.*, 2008) and structural studies on purified complexes (McDermott *et al.*, 1995; Walz *et al.*, 1998; Scheuring *et al.*, 2003; Bahatyrova *et al.*, 2004b; Liu *et al.*, 2008) the circular topographic features are assigned as light-harvesting LH2 complexes. The dimeric features in the AFM topographs arranged in rows (red in Fig. 3A and B) are assigned as RC-LH1-PufX complexes. Previously, we purified this complex, determined its projection structure using cryo-EM and used single particle reconstruction from negatively stained images to obtain a low-resolution 3-D structure for the RC-LH1-PufX dimer (Qian *et al.*, 2005; 2008). The predicted height, derived from these structural and modelling studies of the RC-LH1-PufX core dimer, from the lowest part of the surrounding LH1 ring on the periplasmic face to the highest point on the RC-H subunit is 11.2 nm, and the

distance between the highest points of the two RC-H subunits within a dimer is 10.8 nm. Two sections (the blue lines in Fig. 3A and B) across representative core dimers are shown in Fig. 3C and D. The average height of each RC-H subunit with respect to the mica substrate is 10.1 ± 0.5 nm ($n = 10$) in Fig. 3A and 8.1 ± 0.9 nm ($n = 44$) in Fig. 3B. We measured an average centre-to-centre separation of 8.8 ± 0.7 nm ($n = 9$) for the dimers in the UPB patch in Fig. 3A and 7.8 ± 1.1 nm ($n = 24$) for the ICM patch in Fig. 3B. These variations in heights and distances between the values predicted from the structural model and those measured in UPB and intracytoplasmic membranes are likely to arise from a flattening of the bent dimer structure for both the UPB and ICM and possibly also deformation of the C-terminal region of the α polypeptides of the portion of the LH1 ring that is in contact with the mica in the ICM sample. The two halves of the purified RC-LH1-PufX dimer are inclined at an angle of 146° (Qian *et al.*, 2008); we calculate that an increase to 152° would be sufficient to account for the UPB measurements. This process brings the RC-H subunits approximately 2 nm closer together, and lowers the heights of these subunits above the mica surface by between 0.2 nm (UPB; Fig. 3E, middle) to 0.6 nm (ICM; Fig. 3E, right). The difference between these measurements reflects the greater curvature of the UPB membrane on mica, compared with the ICM where the more extensive LH2-rich membrane regions surrounding the dimers promote stronger adhesion, and hence flattening, onto the mica surface. Given the differing environments of the core dimer complex, either as detergent-purified isolated complexes (Qian *et al.*, 2005; 2008), or as an *in situ* complex in a membrane fragment, there is reasonable correspondence between the structural and AFM data. We conclude that RC-LH1-PufX dimers are present in both the UPB precursor and ICM mature membranes.

The topograph of an ICM patch in Fig. 3B shows that there are more LH2 molecules present than in the UPB, in agreement with absorption spectra of bulk membrane samples (Hunter *et al.*, 1979a). There are rows of RC-LH1-PufX dimers (red), which act as the recipients for solar energy initially absorbed by the smaller LH2 rings, one of which is indicated by an arrow. The UPB membrane, imaged here for the first time by AFM, is less well defined than the ICM in terms of readily recognizable LH2 and RC-LH1-PufX dimer complexes. Nevertheless, the AFM topograph in Fig. 3A shows that the RC-LH1-PufX complexes have dimerized and are organized into a single linear array. Computational studies have shown that a RC-LH1-PufX dimer molecule imposes curvature on the surrounding lipids (Hsin *et al.*, 2009); the presence of several dimers in the UPB (Fig. 3A) suggests that one of the early events in the biogenesis of the ICM of *Rba. sphaeroides* is the promotion of membrane curvature by the combined effects of several closely packed dimers.

Spectral fluorescence imaging of isolated membranes demonstrates a lesion in excitation energy transfer in the immature UPB fraction

Although AFM reveals the organization of the protein complexes that comprise UPB membranes and ICM vesicles, the lateral resolution of this technique is not sufficient to allow predictions of energy transfer characteristics unless there are clear separations between complexes. Förster resonance energy transfer (FRET) is better suited to reveal subtle changes in coupling between proteins, because of the strong, sixth power distance dependence of the resonance energy transfer process (Piston and Kremers, 2007). FRET is used often as an indicator of proximity between donor and acceptor proteins, most commonly employing fluorescent labelling with either dyes or proteins to compensate for the lack of intrinsic chromophores in the system under study. For photosynthetic complexes, the chlorophyll chromophores are ideally suited to act as reporters for the associations between membrane protein complexes, using a FRET-based approach.

In order to compare immature UPB and mature ICM, in terms of energy transfer from LH2 to LH1 complexes, isolated membranes were immobilized onto a glass slide coated with *N*-[3-(trimethoxysilyl)propyl]-ethylenediamine. We used a home-built confocal fluorescence microscope (Kassies *et al.*, 2005) which focuses 800 nm light from a diode laser onto the membranes. The rationale of the experiment is that 800 nm excitation delivers energy to the LH2 complexes present in the membrane; if these complexes are connected to one another and to the RC-LH1-PufX complexes, the excitation energy will migrate through a series of FRET steps in an energetically 'downhill' manner, and will eventually be emitted from the LH1 component of the RC-LH1-PufX complexes. If there is a lesion in energy transfer caused by a physical interruption of energy migration pathways, then there will be disproportionately more emission from the 'uphill' LH2 complexes. The fluorescence signal was detected with a liquid nitrogen-cooled CCD camera which records a complete emission spectrum for every pixel in the image. The fluorescence images of discrete UPB membranes and ICM vesicles are displayed in Fig. 4; each membrane appears as a red patch in Fig. 4A and B. The size of each patch does not correspond to the actual size of a given membrane, since each fluorescence image is diffraction-limited to approximately 400 nm. Figure 4, panels C and D, shows a typical fluorescence emission spectrum from either a single UPB membrane or an ICM vesicle (emission profile in blue), compiled from all of the pixels that comprise a

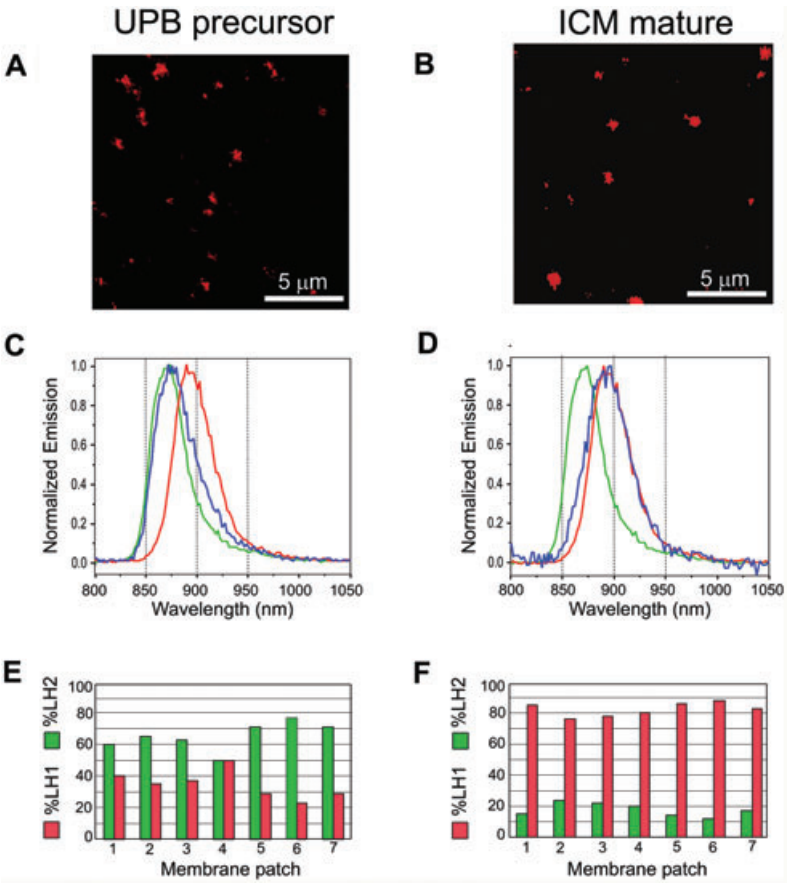

Fig. 4. Spectral fluorescence imaging of FRET in individual UPB membranes and ICM vesicles.
A and B. Confocal microscope images of immobilized, fluorescent UPB and ICM respectively.
C and D. Examples of normalized fluorescence emission spectra of membranes in (A) and (B) (blue lines). Emission spectra of purified membranes from an LH2-only mutant (green line), and from an LH1-only mutant (red line) are included as controls.
E and F. LH2/LH1 emission ratio for a series of individual UPB membranes and ICM vesicles; the analysis was not restricted to the membranes highlighted in (A) and (B). Green is the relative emission from LH2; red the emission from LH1, calculated from the spectra represented by blue lines in (C) and (D).

particular membrane image. We also recorded fluorescence emission spectra as controls, with purified LH2-only membranes (emission profile in green, to represent the extreme case of no LH2-to-LH1 transfer), and LH1-only membranes (emission profile in red, to represent the other extreme where all the energy from LH2 is transferred to, and emitted by, LH1).

There are very clear differences between the UPB and ICM. The fluorescence emission spectrum for one of the ICM vesicles (Fig. 4D) closely matches that of the red LH1 control, indicating that most of the excitation energy delivered to the membrane emerges from the terminal emitter, LH1. In contrast, the emission maximum of the UPB membrane (Fig. 4C) is clearly shifted to lower wavelengths and no longer matches the LH1 emission spectrum. This arises because there is now a greater contribution from LH2 emission, indicating that some of the LH2 complexes in the UPB membrane are uncoupled from their LH1 energy acceptors.

The data from seven membrane patches (UPB) or seven vesicles (ICM) are summarized in the histograms in Fig. 4E and F. A fitting routine was implemented in which the measured emission spectrum for each membrane patch was fitted as a linear combination of spectra from LH2-only and LH1-only membranes. The data have been normalized, but allow a comparison of the relative extents of fluorescence emission from immature and mature membranes. It is clear that there is a consistency from membrane to membrane in the case of mature ICM and also that the major emission in each membrane is from LH1 (red bars, Fig. 4F; data from only 7 of the 14 membranes are shown), because of efficient energy transfer from LH2. The average percentage emission from LH2 is 15.3 ± 4.3 and from LH1 it is 84.7 ± 4.3 ($n = 14$). For the immature UPB membranes, however, the lesion in FRET between LH2 and LH1 produces much higher relative emission from LH2 complexes (green bars, Fig. 4E). For the UPB membranes examined the average percentage emission from LH2 is 65.3 ± 8.8 and from LH1 it is 34.7 ± 8.8 ($n = 7$).

Identification of budded invaginations of the CM, and 'free-living' ICM organelles in the bacterial cytoplasm

The data show that UPB and ICM represent distinct stages in membrane budding, and that they have different morphologies in their purified state, with the UPB precursor membrane forming open, near-hemispherical discs, in marked contrast to the spherical ICM vesicles. The extent to which these differences reflect their respective mor-

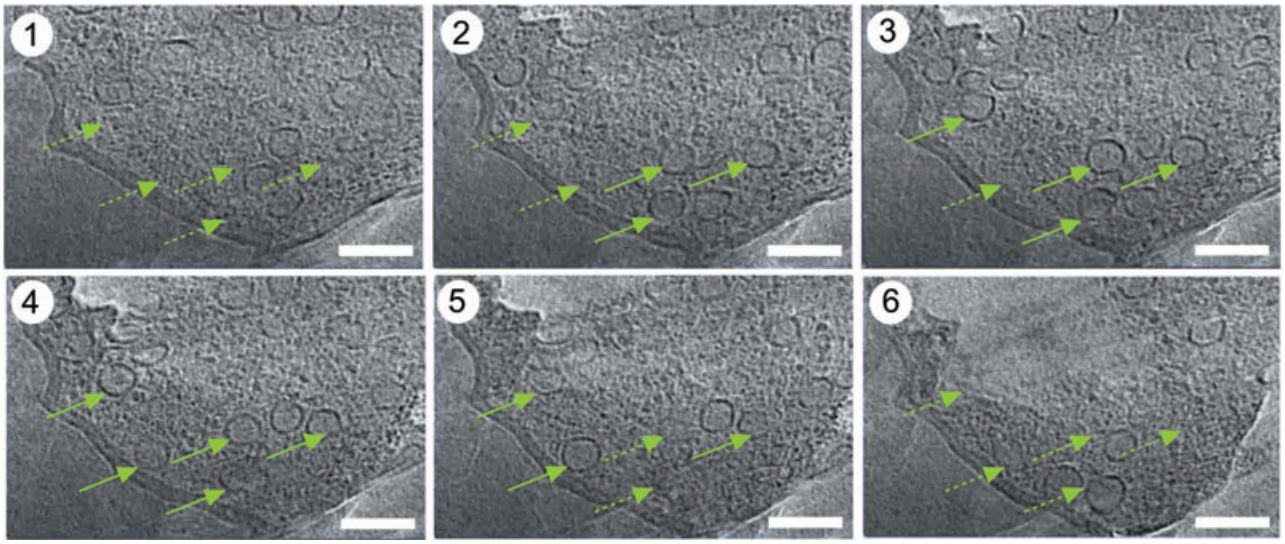

Fig. 5. Cryo-electron tomography of frozen-hydrated sections of *Rba. sphaeroides* cells. Sequential but non-consecutive images (1–6), processing along the *z*-axis, sampling approximately 60 nm of a 150-nm-thick tomographic volume of a frozen-hydrated *Rba. sphaeroides* cell section. Dashed green arrows denote the position of a vesicle that appears in later images and its position after it no longer appears in the tomographic slice; solid green arrows indicate the vesicle when it is clearly visible in a particular cryo-section. Scale bars, 100 nm.

phologies *in vivo* can only be determined by electron tomography of photosynthetically grown *Rba. sphaeroides* cells frozen in a near-native state, with no dehydration, flattening or negative staining. Accordingly, frozen-hydrated cells were cryo-sectioned to yield ribbons of 70 nm nominal thickness, and tilt series from –60° to +60° in 1° tilt increments were acquired. The reconstructed 3-D tomogram volumes reveal well-contrasted internal membranes that correspond to the purified UPB and ICM fractions. Figure 5 shows a sequential, but non-consecutive, series of ~1.8 nm sections along the *z*-axis processing through the tomographic volume, which is approximately 150 nm thick. The vesicle locations are indicated by green arrows; in each case a dashed arrow identifies the location of vesicle that subsequently appears in the following panels, at which point it is denoted using a solid arrow. Finally, the resumption of a dashed arrow shows that the tomographic section has moved through that particular vesicle, and it is no longer visible. Images 1–6 in Fig. 5 are stills from a movie which is included in *Supporting information*; they sample only part of the tomographic volume, and account for approximately 60 nm in the *z* direction, of the 150 nm total. We observed a small amount of compression of the vesicles along the cutting axis, so these stills process through enough of the tomographic volume to pass completely through an ICM vesicle. We conclude that the internal membranes within this cryo-section taken from the interior of the cell are spherical with a diameter of ~50 nm and that they are not attached to the CM, which is closely appressed to the cell wall. It appears that the cytoplasm is occupied by numerous membrane vesicles which house the membrane protein complexes that convert light into ATP, namely the LH2 light-harvesting complex, the RC-LH1-PufX core dimer complex, the cytochrome bc_1 complex and the ATP synthase.

In order to extend our knowledge of internal membrane structure in this bacterium cryo-electron tomography was performed on plunge-frozen whole cells. The thickness and shape of the whole cells prevented the use of high tilt angles during acquisition, so a tilt series from –45° to +45° was acquired, in 2° tilt increments, which resulted in selectively poorer resolution along the *z*-axis. As a result, we could only resolve features in the thinner sample areas, relatively close to the CM, which is closely appressed to the cell wall. Nevertheless, it is clear from examining two 1.8-nm-thick slices from the tomogram volume (Fig. 6A) that there are near-spherical budded membrane structures joined to the CM by a 'neck' (red arrows) prior to budding and complete separation to form the spherical structures (green arrows).

Figure 6A shows two frames from the whole cell tomogram; a more complete analysis of the membrane architecture was enabled by manual segmentation of the tomogram volume. As mentioned previously the data acquisition limitations imposed by using intact, whole cells confined the segmentation to membranes near to the cell wall, so the organization of more centrally located membranes could not be resolved. Due to the limited tilt series used during data acquisition, missing wedge artefacts are apparent in the tomogram volume. These can be observed as an anisotropic degradation of resolution, resulting in a smearing of information along the *z*-axis and lending a columnar aspect to the internal membrane vesicles. A surface-rendered model of the internal mem-

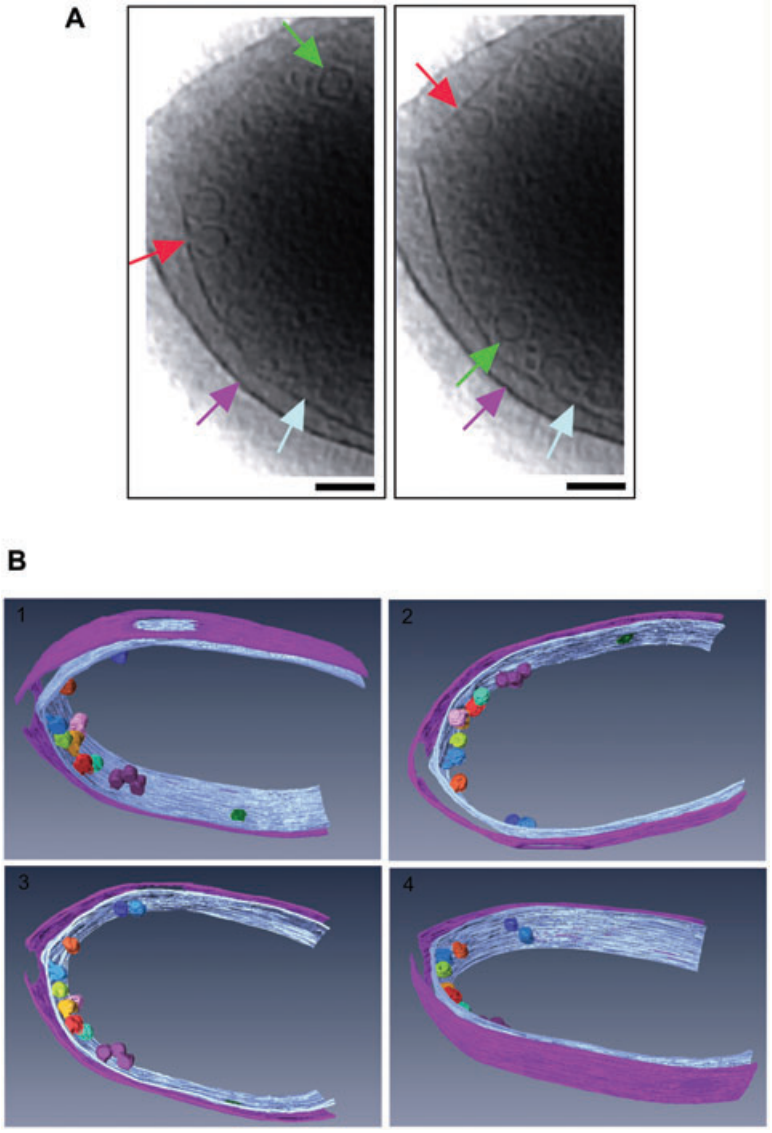

Fig. 6. Cryo-electron tomography of plunge-frozen *Rba. sphaeroides* cells.
A. Two non-consecutive 1.8 nm slices through the tomogram volume are presented. Red arrows indicate membrane invaginations contiguous with the CM. Green arrows indicate budded vesicles apparently fully detached from the CM. Magenta arrow – cell wall; pale blue arrow – CM. Scale bar, 100 nm.
B. Four orientations of a three-dimensional model of the partial internal membrane structure of *Rba. sphaeroides*, generated by segmentation of a tomogram volume. The cell wall is shown in magenta and the CM is shown in pale blue. These membranes are separated by the clearly resolved periplasmic space. Membrane invaginations have been assigned various colours; a dark green-coloured invagination, relatively isolated from the others, panels 1 and 2, is plausibly a UPB. Other invaginations are coloured to distinguish them from one another. All have a connection to the CM. The membrane coloured in purple consists of linked invaginations, of which at least one invagination is still contiguous with the CM.

branes close to the CM was manually segmented (Fig. 6B). Four orientations of this 3-D model are shown, which reveal several types of internal membrane structure, from membranes early in the budding process (dark green), to ICM structures that retain only an indirect connection with the CM anchor point (purple and orange/pink). Moving from the thin periphery (UPB/ICM) to the interior (only ICM), however, the increased sample thickness hinders our ability to resolve internal features. Thus, it is difficult to definitively assign 'true' ICM with the clarity seen in Fig. 5, which was obtained from tomographic analysis of a frozen-hydrated cell section. Although most of the vesicles within the whole cell tomographs cannot be resolved we estimate that, based on diameters in the range 50–55 nm and the vesicle distribution in the cytoplasm, there will be approximately 300 vesicles per cell in the cells examined.

Discussion

Partitioning into smaller membrane-enclosed compartments is a common feature of eukaryotic cells, but such compartments are generally not found in prokaryotes. However, the possibility of membrane organelles does exist in at least some photosynthetic bacteria, which elaborate ICM as infoldings of the CM (Niederman, 2006). *Rba. sphaeroides* provides a well-characterized developmental model for the investigation of membrane invagination, and the mature ICM are particularly well studied; a combination of electron microscopy, AFM, crystallographic and spectroscopic data has allowed the *in silico* construction of an atomic-level model of a complete ICM vesicle, comprising over 150 membrane protein complexes (Sener *et al.*, 2007). However, the biosynthetic processes that initiate the curvature of the CM, and sub-

sequent budding to produce intracytoplasmic structures, are not known; in this work we have used radiolabelling, electron, atomic force and fluorescence microscopy methods, and cryo-electron tomography to examine the early events in ICM formation.

Initiation of membrane budding at the CM

When *Rba. sphaeroides* cells are disrupted by passage through the French press cell the shear forces break the continuity of the cell membrane and three regions, the unpigmented CM, the ICM, and the ICM precursor, the UPB, can all be isolated from cell extracts (Parks and Niederman, 1978; Niederman *et al*., 1979; Inamine *et al*., 1984; Reilly and Niederman, 1986). Apparently, cell disruption and subsequent purification severs the curved UPB membranes from the surrounding CM. The UPB and ICM migrate as two bands in rate-zone sucrose gradients (see Fig. 1), probably as a result of their differing membrane morphologies; the spherical nature of ICM has been known for many years (see Worden and Sistrom, 1964, for example). The present work shows that UPB membranes can be isolated and purified as broadly circular discs (Fig. 2), providing the rationale for the differing migration rates of precursor and mature invaginated membranes that formed the basis of the discovery of Niederman and co-workers, using pulse-labelling experiments, that the UPB is the biosynthetic precursor of the ICM (Niederman *et al*., 1979).

The AFM images in Fig. 3 show that the precursor UPB membrane contains RC-LH1-PufX dimers, which at least in part account for the domed appearance of the UPB membrane in the TEM analysis in Fig. 2. The RC-LH1-PufX dimer complex is a membrane bending protein, by virtue of the 146° angle subtended on the periplasmic side of the membrane by the two monomer halves of the complex (Qian *et al*., 2008). The consequence of genetically manipulating *Rba. sphaeroides* so that it assembles RC-LH1-PufX dimers, but no LH2, is the formation of tubular ICM with an average diameter of 70 nm (Hunter *et al*., 1988; Kiley *et al*., 1988; Siebert *et al*., 2004). This property of the core dimer places it in the same category as other intrinsic membrane proteins that are known to impose curvature on the membrane, such as the nicotinic acetylcholine receptor (Miyazawa *et al*., 2003), and the ATPase (Dudkina *et al*., 2006). The initiation of membrane curvature (McMahon and Gallop, 2005) has been studied using coarse-grained simulations (Reynwar *et al*., 2007), and the model membrane system presented here has also been studied computationally using Monte Carlo simulations (Frese *et al*., 2008). A plausible first event that introduces curvature within an initially flat CM is the association of dimeric core complexes, driven by the size and shape mismatch between bent RC-LH1-PufX dimers and surrounding membrane proteins (Frese *et al*., 2008). Once formed, core RC-LH1-PufX dimer arrays will distort the surrounding lipids and possibly assist the insertion of further pigment protein complexes; this process has been studied in detail using a novel molecular dynamics flexible fitting method (Hsin *et al*., 2009). The limited arrays of core dimers in the AFM topograph of a UPB membrane in Fig. 3A are in agreement with fluorescence yield measurements, which showed that membranes at the earliest stages of development consist of ordered aggregates of LH1 complexes that interconnect and surround three to six RCs, equivalent to one to three core dimers (Hunter *et al*., 1985). This sequence of membrane development, which predicts that the assembly of cores precedes the incorporation of LH2 complexes, is consistent with previous work by Niederman and co-workers that demonstrated the stepwise formation of ICM, with LH2 incorporation lagging behind that of the core RC-LH1-PufX complexes (Niederman *et al*., 1976; Koblizek *et al*., 2005).

The onset of membrane invagination must involve the close interplay between the pigment biosynthetic enzymes that catalyse BChl and carotenoid pigment synthesis, lipid biosynthesis enzymes, and the genes encoding apoproteins of membrane protein complexes that convert light into ATP. The UPB precursor membrane is enriched in bacteriochlorophyll synthase, and has a high level of BChl biosynthesis activity, shown using the radiolabelled BChl precursor H^3-δ-aminolevulinic acid (Hunter *et al*., 2005). Co-ordination of these biosynthetic reactions originates in the global control circuits mediated by light and oxygen-responsive two-component sensor-regulator proteins (Bauer *et al*., 2008; Klug and Masuda, 2008). Thus, it is reasonable to suggest that the UPB membrane will have a composition, in terms of biosynthetic, regulatory and nascent photosynthetic complexes, that is distinct from the surrounding CM, which is known to be enriched in respiratory complexes (Parks and Niederman, 1978). This proposed discontinuity in protein and/or lipid composition between these early invagination sites and the surrounding CM could account for the roughly circular shape of the UPB, as it shears from its surrounding CM during cell disruption in the French press.

The membrane-by-membrane analysis of the fluorescence emission spectra (Fig. 4E) shows the individual behaviour of each UPB fragment, with none of those examined showing the efficient LH2-core dimer energy transfer typical of mature ICM vesicles. This analysis updates a much earlier observation of this energy transfer behaviour using bulk membrane samples (Hunter *et al*., 1979b). The analysis of fluorescence in individual membranes in Fig. 4 shows that the LH2 complexes in the UPB membrane are imperfectly connected to the RC-LH1-PufX dimers for energy transfer. The stringent distance

constraints for FRET reveal these imperfect connections, whereas the lateral resolution of AFM, particularly as applied to the analysis of these curved UPB membranes in Fig. 3A, does not provide sufficient structural detail. This lesion in energy transfer leads to an elevated fluorescence emission from at least some of the LH2 complexes in the UPB membrane. In contrast, the mature ICM contains a greater proportion of LH2 (see the AFM images in Fig. 3B), all of which has integrated efficiently into the membrane to allow efficient energy transfer to RC-LH1-PufX core dimers. This greater LH2 content with respect to the UPB is a feature of the mature ICM from cells grown at a variety of light intensities; although cellular levels of LH2 antenna are elevated at low-light growth conditions, this increase is restricted to the ICM fraction, whereas the LH2 content of the precursor UPB membrane is held at lower and constant levels (Hunter *et al*., 2005). It is not clear why at least some of the LH2 complexes that are present in the UPB are imperfectly connected for excitation energy transfer. The LH2 complex is a known driver of membrane curvature (Hunter *et al*., 1988; Chandler *et al*., 2008; Olsen *et al*., 2008), and it is possible that the assembly, stability and energy transfer function of LH2 are not optimized in the UPB precursor membrane because of curvature mismatch between the LH2 and core dimer complexes (Frese *et al*., 2008). Another more straightforward explanation for imperfectly coupled energy transfer to RC-LH1-PufX cores is physical obstruction of optimal LH2-core dimer contacts by the presence of biosynthetic pathway and assembly factor proteins; such 'non-photosynthetic' proteins are a significant feature of the protein composition of the UPB (H.J. Lewis *et al*., in preparation).

Distinct populations of internal membranes in Rba. sphaeroides *cells*

The cryo-electron tomography data, recorded from both cell sections and whole cells of *Rba. sphaeroides*, reveal at least four physically distinct types of internal membrane. A fascinating picture of ICM proliferation emerges; some ICM vesicles are truly 'free-living' inside the bacterial cytoplasm (Fig. 5), fitting the description of an organelle in the sense that they are specialized membrane-enclosed structures which house chemical and metabolic functions central to the function of the cell. More specifically, the ICM vesicle is a basic minimal unit for photosynthetic ATP formation. In contrast, those ICM found nearer to the cell wall-appressed CM (Fig. 6B) sometimes form interconnected fused structures, often retaining a connection to the CM and possibly having access to the periplasmic space. Near-spherical single invaginations are also observed, still attached to the CM by a 'neck' (Fig. 6A). A tomographic study of *Blastochloris viridis* cells also revealed that narrow tubular structures maintain continuity between the lamellar ICM and the CM (Konorty *et al*., 2008).

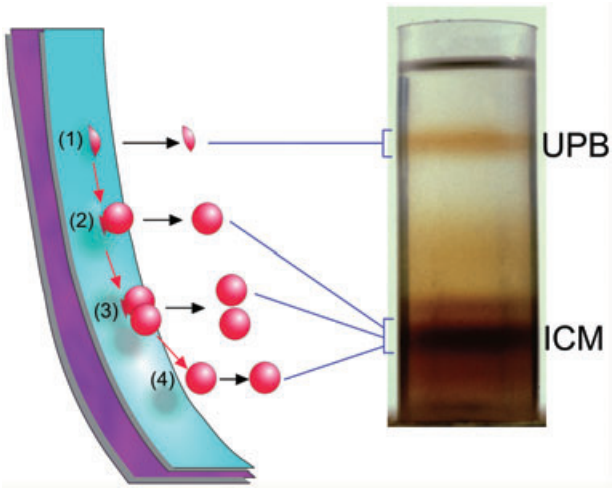

Fig. 7. Diagrammatic representation of the cellular origins of UPB and ICM vesicles, and their separation in a rate-zone sucrose density gradient. The cell wall is depicted in magenta and the cytoplasmic membrane (CM) in cyan. Invaginations of the CM are shown in red. The diagram depicts snapshots from a possible developmental sequence (red arrows). Disruption of the cell in a French press (black arrows) produces the membrane structures shown, which migrate to one of two positions in the 5–35% w/w sucrose density gradient (blue lines).
(1) Small indentations of the CM, representing the earliest stages of membrane budding, form the top band in the gradient (pictured).
(2) Further invagination of the UPB produces a more curved, budded membrane, which forms a sealed spherical vesicle upon cell disruption.
(3) A second budding event can be initiated within the ICM which produces an interconnected 'double' vesicular structure. However, upon cell breakage two separate structures form.
(4) The budded structures in either (2) or (3) can be released into the interior of the cell to form spherical vesicles.

Finally, we observed small indentations of the CM, representing the earliest stages of membrane budding. These resemble the indentations of the CM seen in freeze-fracture analysis of *Rba. sphaeroides* cells undergoing a transition from chemoheterotrophic to photoheterotrophic growth conditions (Chory *et al*., 1984). The tomography analysis therefore reveals a continuum of structures which represent snapshots from a developmental sequence (Fig. 7, red arrows); this process culminates with the release of spherical intracytoplasmic vesicles into the interior of the cell. The diagram in Fig. 7 relates the membrane structures observed in the tomography analysis to their positions in the rate-zone sucrose density gradients, which form the basis for the pulse-chase analysis in Fig. 1. This density gradient method can distinguish between the disc-like UPB sites where the membrane invagination process is initiated, but following cell disruption (black arrows) the ICM fraction can arise either from budded ICM still attached to the CM, from

interconnected ICM vesicles, or from vesicles completely detached from any other cellular structure. The rate-zone sucrose density gradients used in this and previous work by Niederman and colleagues (Parks and Niederman, 1978; Niederman *et al*., 1979; Inamine *et al*., 1984; Reilly and Niederman, 1986) separate structures based on the rate at which they sediment rather than their density, so the size and shape of the membranes influence the banding pattern. The two major membrane morphologies, open patches (UPB) and spheres (ICM; see Fig. 7), produce two distinct bands in such gradients. In order to provide more surface area for light absorption and photochemistry, existing membrane invaginations need to grow; it appears that a secondary budding process can be initiated within an existing invagination. The alternative would be for a single bud to become larger, but this would require a progressive reduction in membrane curvature that would be resisted by the 146° bend in the RC-LH1-PufX dimer, which imposes a maximum diameter of approximately 70 nm on the membrane that houses it (Qian *et al*., 2008; Hsin *et al*., 2009). Secondary budding conserves the 70-nm-diameter membrane curvature, but permits further invagination of an existing bud. As membrane biogenesis proceeds, driven by continued synthesis of lipids and membrane protein complexes, at least some of the buds become completely detached from their CM or ICM anchor points and are released into the interior of the cell to form spherical vesicles. It is likely that the proportion of detached ICM vesicles will increase in cells grown under low-light conditions.

The issue of whether or not there are free vesicles in the cytoplasm of photosynthetic bacteria, or whether some or all of these membranes retain a connection with the CM goes back over 50 years in the literature. Comparisons with work conducted on different photosynthetic bacteria, grown under a variety of aeration regimes and light intensities, and with membranes prepared following a variety of cell disruption methods are difficult, and outside the scope of this *Discussion*. However, Gibson (1965a,b) and Collins and Niederman (1976), for example, demonstrated that at least part of the intracytoplasmic vesicle population in cells is structurally independent of the CM. Often, such conclusions were reached on the basis of experiments on spheroplasts, which was reasonable given that gentle osmotic lysis of cell wall-free structures was more likely to reflect the internal membrane morphology than analysis of material mechanically disrupted by passage through a French pressure cell. However, even spheroplast preparation is not without its drawbacks; previously intact structures are still disrupted and often the procedure involves the use of a non-ionic detergent such as Brij-58, so one cannot be sure that ICM do not open then reseal during membrane preparation. Prince *et al*. (1975) showed that up to 85% of the *c*-type cytochrome originally present in photosynthetically grown cells of *Rba. sphaeroides* was liberated during preparation of spheroplasts, suggesting that fused intracellular membranes are present and that there is a continuum between the periplasm and the periplasmic face of the population of ICM. The tomographic data in Fig. 6B show that such fused structures do exist, and that they can retain a connection with the CM and the periplasmic space. One of the invaginated models in Fig. 7, identified by the number (3), depicts one of these conjoined invaginations. However, we cannot quantify the proportion of membranes that retain a connection with the periplasm, and only note that both CM-connected and free ICM exist, and that the ratio of connected to free structures is likely to vary, with more free ICM present at lower light intensities. The tomography work reported here on cryo-frozen material avoids cell disruption and any dehydration or staining procedures, and is likely to reflect the native state of the intact cell.

It is not yet possible to construct a full 3-D tomographic model of the interior of an entire, intact *Rba. sphaeroides* cell owing to the limitations imposed by the > 0.5 μM thickness of bacterial cells (Konorty *et al*., 2008; Brandt *et al*., 2009). However cryo-tomography of frozen-hydrated cell sections clearly shows that there are numerous spherical vesicles within the cell. The volume of the cytoplasm enclosed by an $800 \times 800 \times 2000$ nm bacterial cell can be calculated as approximately 7×10^8 nm^3; the occupancy of the bacterial cytoplasm is reflected in the number of circular membrane sections identified in the tomographic slices in Fig. 5, where approximately 15% of the cytoplasm contains vesicles. When extrapolated to a whole cell, we calculate that there are approximately 800 ICM vesicles per cell. This figure can fluctuate significantly depending on the light intensity and oxygen tension at which the cells are grown (Worden and Sistrom, 1964; Cellarius and Peters, 1969; Niederman *et al*., 1976). Nevertheless, in broad terms, the figure of 800 agrees with the range of 140–640 vesicles per cell, estimated from the BChl content of whole cells and the number of functionally connected pigments (3000) in a single vesicle (Hunter *et al*., 1985). This latter number was also used as the basis for constructing atomic-level models of ICM vesicles (Sener *et al*., 2007).

The ICM vesicles are prokaryotic organelles, which consist of a physically and functionally interconnected series of membrane protein complexes that carry out a core function of the cell, namely converting solar energy into ATP. LH and RC complexes in the ICM first convert light energy into a stable charge separation and subsequently to the reduced state of a mobile electron carrier, ubiquinol-10. Reduced quinones migrate to the cytochrome bc_1 complex, where protons are injected into the lumen of the vesicle. Geyer and Helms (2006) calculate that as few as 60 'free' protons confined within an ICM vesicle create a

transmembrane pH gradient of 3.4. Controlled dissipation of this pH gradient through the proton channel of the ATPase, which can consume as many as 400 protons per second, captures the solar energy in a chemical form as ATP. It is interesting to note that ICM curvature, driven in part by the 146° bend in the $(RC\text{-}LH1\text{-}PufX)_2$ dimer (Qian *et al*., 2008), creates a spherical structure with a 50–70 nm diameter. It is possible that this is an optimal surface area : volume ratio, a compromise between increasing the number of complexes for light absorption, energy and electron transfer, while needing to constrain the internal volume of the vesicle, so that the proton gradient is large enough to drive ATP synthesis. The construction of atomic-level models for these membrane vesicles will, one day, allow the whole process, from light to ATP, to be modelled *in silico*. This approach is still at an early stage, but the model constructed (Sener *et al*., 2007) has already made some predictions about the overall efficiency of energy trapping that can be tested by experiment. Further developments would include lipids in the model, which is currently assembled from only a few types of protein: the LH complexes, the RC, the cytochrome bc_1 complex and the ATP synthase. Proteomic analyses conducted highlight the real complexity of these vesicles, which contain a total of 98 different proteins (Zeng *et al*., 2007). Thus, construction of a complete model of the whole membrane is a significant challenge. However, the progress illustrated by this work on the structural and functional analyses of the precursor UPB membrane might lead to atomic-level models of the earliest stages of membrane assembly and curvature.

Experimental procedures

Cell culture and membrane preparation

Rhodobacter sphaeroides NCIB 8253 was grown photosynthetically at a light intensity of 600 μmol s^{-1} m^{-2} in CB medium (Cohen-Bazire *et al*., 1957). Five grams of cells suspended in 10 ml of 1 mM Tris-HCl pH 7.5, 1 mM EDTA were disrupted by two cycles of French pressing at 18 000 p.s.i. The cell extract was fractionated by rate-zone centrifugation at 96 000 *g* for 4 h on a 5–35% (w/w) sucrose gradient in 1 mM Tris-HCl pH 7.5, 1 mM EDTA. UPB and ICM vesicle fractions were recovered for further analysis.

UPB purification

Following dialysis against 1 mM Tris-HCl, pH 7.5, 1 mM EDTA to remove sucrose the UPB was fractionated on a 5–15% (w/w) sucrose gradient containing 20 mM Tris-HCl pH 7.5, 20 mM EDTA layered onto a 60% (w/w) sucrose cushion and centrifuged at 100 000 *g* for 10 h. The membrane band at the interface between the cushion and the gradient was harvested.

Pulse-chase radiolabelling experiments

Rhodobacter sphaeroides NCIB 8253 was grown photosynthetically with N_2 sparging. Cells ($absorbance_{680} = 0.7$) were pulsed with a final concentration of 0.2 μCi ml^{-1} S^{35} L-methionine (Easytag™, PerkinElmer) for 5 min before a 10^4-fold excess of unlabelled L-methionine was added as a chase. Samples (250 ml) were removed from the culture at intervals during the chase and mixed with 160 μM chloramphenicol and protease inhibitor cocktail (Complete™, Roche). UPB and ICM fractions, prepared as detailed above, were mixed with scintillation solution (FluoranSafe2™, BDH chemicals) and analysed in a scintillation counter (Beckman Coulter, LS6500).

TEM of membranes

Isolated membrane fragments were applied to glow-discharged carbon-coated copper grids (400 mesh, Agar Scientific), negatively stained with 0.75% (w/v) uranyl formate and examined with a Phillips CM100 electron microscope. Images were recorded using an in-line 1K Gatan Multiscan 794 CCD camera.

Atomic force microscopy

Atomic force microscopy imaging was carried out with a Veeco Nanoscope IV AFM equipped with an 'E' scanner (15×15 μm). Sharpened SiN (NPS) cantilevers ($k = 0.06$ N m^{-1}) (Veeco) were used in a standard Veeco tapping mode fluid cell operating at 6–10 kHz. Tip-sample interaction forces were kept minimal while imaging. Images were recorded at scan frequencies of 0.5–1.5 Hz. For imaging UPB membranes were adsorbed for 1 h onto freshly cleaved mica (Agar Scientific) in 20 mM HEPES, pH 7.5, 150 mM KCl, 25 mM $MgCl_2$, 5 mM $NiSO_4$. ICM vesicles were opened to form patches for AFM imaging using 0.01% (w/v) β-dodecyl maltoside (Glycon Biochemistry, GmbH Biotechnology, Germany) as described previously (Bahatyrova *et al*., 2004a). For low-resolution imaging membranes were adsorbed for 20 min onto freshly cleaved mica (Agar Scientific) in 20 mM HEPES, pH 7.5, 150 mM KCl, 25 mM $MgCl_2$. Low tapping amplitudes were used. Images (512×512 pixels) were processed using the Nanoscope (v6.14R1) software and Vision (v4.10) software (Veeco).

Fluorescence imaging of single membrane patches and vesicles

Fluorescence emission data were acquired using a home-built confocal microscope (Kassies *et al*., 2005). Substrates (microscope coverslips, Menzel-glaser # 1) were cleaned by immersion in piranha solution (3:1 concentrated H_2SO_4/33% aqueous H_2O_2) for 15 min and dried with nitrogen. The surface was modified with *N*-[3-(trimethoxysilyl)propyl]-ethylenediamine. Two microlitres of sample solution, containing either UPB membranes or ICM vesicles, was applied to the substrate followed by the addition of 100 μl of the adsorption buffer (10 mM Tris-HCl pH 7.5, 150 mM KCl, 25 mM $MgCl_2$) for 15 min. Later the samples were rinsed copiously

with the imaging buffer (10 mM Tris-HCl pH 7.5, 150 mM KCl) and kept under liquid conditions during measurement. Fluorescent images consisted of 128 × 128 pixels. Spectral information was acquired with 100 ms acquisition time and 6 μW excitation power measured at the back aperture of the objective. Data were analysed by application of a fitting routine, in which the measured spectra for each membrane patch are fitted as a linear combination of LH2-only and LH1-only membranes.

Cryo-electron tomography

Rhodobacter sphaeroides NCIB 8253 was grown photosynthetically (100 μmol s^{-1} m^{-2}) in 30 ml bottles. Cells were harvested by centrifugation at 10 000 *g* for 10 min, washed and resuspended in growth medium at an appropriate concentration for plunge freezing experiments or resuspended in a minimal volume of growth medium for high-pressure freezing.

Plunge frozen cells. A 5 μl aliquot of *Rba. sphaeroides* was applied to freshly glow-discharged 300 mesh carbon-coated Quantifoil multi-A grids, blotted in a humid atmosphere then plunged into liquid ethane (Dubochet *et al*., 1988). Grids were stored under liquid nitrogen until required.

High-pressure frozen cells. Concentrated samples of *Rba. sphaeroides* were frozen in a Baltec HPM-010 high-pressure freezer as 200-μm-thick films sandwiched between two aluminium planchettes. Any residual air volume was occupied using the osmotically inactive filler compound 1-hexadecene.

Cryo-sectioning of frozen-hydrated samples. Planchettes of high-pressure frozen suspensions of *Rba. sphaeroides* were transferred to the pre-cooled cryo-box of a Leica EM UC6/FC6 ultra-microtome. A ~75 × 75 μm block face was trimmed, faced then cryo-sectioned at a 70 nm nominal thickness using a Diatome 25° cryo platform knife set to a clearance angle of 9°. The cryochamber temperature was set at −160°C and a cutting speed of 0.6 mm s^{-1} was used. Section ribbons were transferred onto glow-discharged carbon-coated Quantifoil copper 200 mesh grids using a Dalmatian dog hair and a Leitz micromanipulator (Ladinsky *et al*., 2006). Section ribbons were pressed with a stamping tool and stored under liquid nitrogen until required.

All data were collected using a JEOL JEM-3200FSC transmission electron microscope equipped with a field emission gun and in-column energy filter at a temperature of 84 K. Images were recorded at a magnification of × 25 000 on a 4 k × 4 k CCD binned twofold corresponding to a sampling of 1.8 nm at the specimen level. Single-axis tilt series were collected using SerialEM (Mastronarde, 2005) with defocuses of −12 to −15 μm and a total dose of ~45 e $Å^{-2}$. Tilt series were acquired from −60° to +60° in 1° tilt increments for frozen-hydrated sections; data were acquired at × 33 962 magnification. For plunge-frozen cells data were acquired at × 26 806 magnification and tilt series acquired from −45° to +45° in 2° tilt increments.

Image processing and segmentation. Fiducial-less tilt series were aligned using Protomo (Winkler, 2007). Tomogram volumes were created by weighted back-projection and denoised with 30 iterations of non-linear anisotropic diffusion (Frank *et al*., 1996; Frangakis and Hegerl, 2001). Denoised tomogram volumes were viewed, analysed and segmented using Amira 4.1.2 (Visage Imaging).

Acknowledgements

J.D.T., J.D.O., C.N.H. acknowledge financial support from the Biotechnology and Biological Sciences Research Council (UK). P.G.A. has a doctoral studentship from the Biotechnology and Biological Sciences Research Council (UK). M.E., C.O. acknowledge financial support from Nanotechnology Network in the Netherlands, NANONED project number 7124. C.A.S. and D.L.S. acknowledge financial support from the New York Structural Biology Centre (USA) and thank Dr Bill Rice for assistance with data acquisition and processing.

References

Bahatyrova, S., Frese, R.N., Siebert, C.A., Olsen, J.D., van der Werf, K.O., van Grondelle, R., *et al*. (2004a) The native architecture of a photosynthetic membrane. *Nature* **430:** 1058–1062.

Bahatyrova, S., Frese, R.N., van der Werf, K.O., Otto, C., Hunter, C.N., and Olsen, J.D. (2004b) Flexibility and size heterogeneity of the LH1 light harvesting complex revealed by atomic force microscopy: functional significance for bacterial photosynthesis. *J Biol Chem* **279:** 21327–21333.

Bauer, C.E., Setterdahl, A., Wu, J., and Robinson, B.R. (2008) Regulation of gene expression in response to oxygen tension. In *The Purple Phototrophic Bacteria*. Hunter, C.N., Daldal, F., Thurnauer, M.C., and Beatty, J.T. (eds). Dordrecht: Springer, pp. 707–725.

Bowyer, J.R., Hunter, C.N., Ohnishi, T., and Niederman, R.A. (1985) Photosynthetic membrane development in *Rhodopseudomonas sphaeroides*. Spectral and kinetic characterization of redox components of light-driven electron flow in apparent photosynthetic membrane growth initiation sites. *J Biol Chem* **260:** 3295–3304.

Brandt, F., Etchells, S.A., Ortiz, J.O., Elcock, A.H., Hartl, F.U., and Baumeister, W. (2009) The native 3D organization of bacterial polysomes. *Cell* **136:** 261–271.

Cellarius, R.A., and Peters, G.A. (1969) Photosynthetic membrane development in *Rhodopseudomomas spheroides*: incorporation of bacteriochlorophyll and development of energy transfer and photochemical activity. *Biochim Biophys Acta* **189:** 234–244.

Chandler, D.E., Hsin, J., Harrison, C.B., Gumbart, J., and Schulten, K. (2008) Intrinsic curvature properties of photosynthetic proteins in chromatophores. *Biophys J* **95:** 2822–2836.

Chory, J., Donohue, T.J., Varga, A.R., Staehelin, L.A., and Kaplan, S. (1984) Induction of the photosynthetic membranes of *Rhodopseudomonas sphaeroides*: biochemical and morphological studies. *J Bacteriol* **159:** 540–554.

Cohen-Bazire, G., Sistrom, W.R., and Stanier, R. (1957) Kinetic studies of pigment synthesis by non-sulphur purple bacteria. *J Comp Cell Physiol* **49:** 25–68.

Collins, M.L.P., and Niederman, R.A. (1976) Membranes of

Rhodospirillum rubrum: physicochemical properties of chromatophore fractions isolated from osmotically and mechanically disrupted cells. *J Bacteriol* **126:** 1326–1338.
Dubochet, J., Adrian, M., Chang, J.-J., Homo, J.-C., Lepault, J., McDowall, A.W., and Schultz, P. (1988) Cryo-electron microscopy of vitrified specimens. *Q Rev Biophys* **21:** 129–228.
Dudkina, N.V., Sunderhaus, S., Braun, H.P., and Boekema, E.J. (2006) Characterization of dimeric ATP synthase and cristae membrane ultrastructure from *Saccharomyces* and *Polytomella* mitochondria. *FEBS Lett* **580:** 3427–3432.
Field, C.B., Behrenfeld, M.J., Randerson, J.T., and Falkowski, P. (1998) Primary production of the biosphere: integrating terrestrial and oceanic components. *Science* **281:** 237–240.
Frangakis, A.S., and Hegerl, R. (2001) Noise reduction in electron tomographic reconstructions using nonlinear anisotropic diffusion. *J Struct Biol* **135:** 239–250.
Frank, J., Radermacher, M., Penczek, P., Zhu, J., Li, Y., Ladjadj, M., and Leith, A. (1996) SPIDER and WEB: processing and visualization of images in 3D electron microscopy and related fields. *J Struct Biol* **116:** 190–199.
Frese, R.N., Olsen, J.D., Branvall, R., Westerhuis, W.H., Hunter, C.N., and van Grondelle, R. (2000) The long-range supraorganization of the bacterial photosynthetic unit: a key role for PufX. *Proc Natl Acad Sci USA* **97:** 5197–5202.
Frese, R.N., Siebert, C.A., Niederman, R.A., Hunter, C.N., Otto, C., and van Grondelle, R. (2004) The long-range organization of a native photosynthetic membrane. *Proc Natl Acad Sci USA* **101:** 17994–17999.
Frese, R.N., Pamies, J., Olsen, J.D., Bahatyrova, S., van der Weij-de Wit, C., Aartsma, T.J., *et al*. (2008) Protein shape and crowding drive domain formation and curvature in biological membranes. *Biophys J* **94:** 640–647.
Geyer, T., and Helms, V. (2006) Reconstruction of a kinetic model of the chromatophore vesicles from *Rhodobacter sphaeroides*. *Biophys J* **91:** 927–937.
Gibson, K.D. (1965a) Nature of the insoluble pigmented structures (chromatophores) in extracts and lysates of *Rhodopseudomonas spheroides*. *Biochemistry* **4:** 2027–2041.
Gibson, K.D. (1965b) Isolation and characterisation of chromatophores from *Rhodopseudomonas spheroides*. *Biochemistry* **4:** 2042–2051.
Hsin, J., Gumbart, J., Trabuco, L.G., Villa, E., Qian, P., Hunter, C.N., and Schulten, K. (2009) Protein-induced membrane curvature investigated through molecular dynamics flexible fitting. *Biophys J* **97:** 321–329.
Hunter, C.N., Holmes, N.G., Jones, O.T.G., and Niederman, R.A. (1979a) Membranes of *Rhodopseudomonas sphaeroides*. VII. Photochemical properties of a fraction enriched in newly synthesized bacteriochlorophyll *a*–protein complexes. *Biochim Biophys Acta* **548:** 253–266.
Hunter, C.N., van Grondelle, R., Holmes, N.G., Jones, O.T.G., and Niederman, R.A. (1979b) Fluorescence yield properties of a fraction enriched in newly synthesized bacteriochlorophyll *a* protein complexes from *Rhodopseudomonas sphaeroides*. *Photochem Photobiol* **30:** 313–316.
Hunter, C.N., Kramer, H.J.M., and van Grondelle, R. (1985) Linear dichroism and fluorescence emission of antenna complexes during photosynthetic unit assembly in *Rhodopseudomonas sphaeroides*. *Biochim Biophys Acta* **807:** 44–51.
Hunter, C.N., Pennoyer, J.D., Sturgis, J.N., Farrelly, D., and Niederman, R.A. (1988) Oligomerization states and associations of light-harvesting pigment protein complexes of *Rhodobacter sphaeroides* as analyzed by lithium dodecylsulfate polyacrylamide-gel electrophoresis. *Biochemistry* **27:** 3459–3467.
Hunter, C.N., Tucker, J.D., and Niederman, R.A. (2005) The assembly and organisation of photosynthetic membranes in *Rhodobacter sphaeroides*. *Photochem Photobiol Sci* **4:** 1023–1027.
Inamine, G.S., Van Houten, J., and Niederman, R.A. (1984) Intracellular localization of photosynthetic membrane growth initiation sites in *Rhodopseudomonas sphaeroides*. *J Bacteriol* **158:** 425–429.
Johnson, Z.I., Zinser, E.R., Coe, A., McNulty, N.P., Woodward, E.M., and Chisholm, S.W. (2006) Niche partitioning among *Prochlorococcus* ecotypes along ocean-scale environmental gradients. *Science* **311:** 1737–1740.
Kassies, R., van der Werf, K.O., Lenferink, A., Hunter, C.N., Olsen, J.D., Subramaniam, V., and Otto, C. (2005) Combined AFM and confocal fluorescence microscope for application in bio-nanotechnology. *J Microsc* **217:** 109–116.
Kiley, P.J., Varga, A.R., and Kaplan, S. (1988) Physiological and structural analysis of light-harvesting mutants of *Rhodobacter sphaeroides*. *J Bacteriol* **170:** 1103–1115.
Klug, G., and Masuda, S. (2008) Regulation of genes by light. In *The Purple Phototrophic Bacteria*. Hunter, C.N., Daldal, F., Thurnauer, M.C., and Beatty, J.T. (eds). Dordrecht: Springer, pp. 727–741.
Koblizek, M., Shih, J.D., Breitbart, S.I., Ratcliffe, E.C., Kolber, Z.S., Hunter, C.N., and Niederman, R.A. (2005) Sequential assembly of photosynthetic units in *Rhodobacter sphaeroides* as revealed by fast repetition rate analysis of variable bacteriochlorophyll *a* fluorescence. *Biochim Biophys Acta* **1706:** 220–231.
Konorty, M., Kahana, N., Linaroudis, A., Minsky, A., and Medalia, O. (2008) Structural analysis of photosynthetic membranes by cryo-electron tomography of intact *Rhodopseudomonas viridis* cells. *J Struct Biol* **161:** 393–400.
Ladinsky, M.S., Pierson, J.M., and McIntosh, J.R. (2006) Vitreous cryo-sectioning of cells facilitated by a micromanipulator. *J Microsc* **224:** 129–134.
Liu, L.-N., Aartsma, T.J., and Frese, R.N. (2008) Dimers of light-harvesting complex 2 from *Rhodobacter sphaeroides* characterized in reconstituted 2D crystals with atomic force microscopy. *FEBS J* **275:** 3157–3166.
McDermott, G., Prince, S.M., Freer, A.A., Hawthornthwaite-Lawless, A.M., Papiz, M.Z., Cogdell, R.J., and Isaacs, N.W. (1995) Crystal structure of an integral membrane light-harvesting complex from photosynthetic bacteria. *Nature* **374:** 517–521.
McMahon, H.T., and Gallop, J.L. (2005) Membrane curvature and mechanisms of dynamic cell membrane remodelling. *Nature* **438:** 590–596.
Mastronarde, D.N. (2005) Automated electron microscope tomography using robust prediction of specimen movements. *J Struct Biol* **152:** 36–51.

Miyazawa, A., Fujiyoshi, Y., and Unwin, N. (2003) Structure and gating mechanism of the acetylcholine receptor pore. *Nature* **423:** 949–955.

Nevo, R., Charuvi, D., Shimoni, E., Schwarz, R., Kaplan, A., Ohad, I., and Reich, Z. (2007) Thylakoid membrane perforations and connectivity enable intracellular traffic in cyanobacteria. *EMBO J* **26:** 1467–1473.

Niederman, R.A. (2006) Structure, function and formation of bacterial intracytoplasmic membranes. In *Complex Intracellular Structures in Prokaryotes*. Shively, J.M. (ed.). Berlin, Heidelberg: Springer-Verlag, pp. 193–227.

Niederman, R.A., Mallon, D.E., and Langan, J.J. (1976) Membranes of *Rhodopseudomonas sphaeroides*. IV. Assembly of chromatophores in low-aeration cell suspensions. *Biochim Biophys Acta* **440:** 429–447.

Niederman, R.A., Mallon, D.E., and Parks, L.C. (1979) Membranes of *Rhodopseudomonas sphaeroides*. VI. Isolation of a fraction enriched in newly synthesized bacteriochlorophyll *a*–protein complexes. *Biochim Biophys Acta* **555:** 210–220.

Olsen, J.D., Tucker, J.D., Timney, J.A., Qian, P., Vassilev, C., and Hunter, C.N. (2008) The organization of LH2 Complexes in membranes from *Rhodobacter sphaeroides*. *J Biol Chem* **283:** 30772–30779.

Parks, L., and Niederman, R.A. (1978) Membranes of *Rhodopseudomonas sphaeroides* V. Identification of bacteriochlorophyll *a*-depleted cytoplasmic membrane in phototrophically grown cells. *Biochim Biophys Acta* **511:** 70–82.

Piston, D.W., and Kremers, G.J. (2007) Fluorescent protein FRET: the good, the bad and the ugly. *Trends Biochem Sci* **32:** 407–414.

Prince, R.C., Baccarini-Melandri, A., Hauska, G.A., Melandri, B.A., and Crofts, A.R. (1975) Asymmetry of an energy transducing membrane. The location of cytochrome c_2 in *Rhodopseudomonas spheroides* and *Rhodopseudomonas capsulata*. *Biochim Biophys Acta* **387:** 212–227.

Qian, P., Hunter, C.N., and Bullough, P.A. (2005) The 8.5 Å projection structure of the core RC-LH1-PufX dimer of *Rhodobacter sphaeroides*. *J Mol Biol* **349:** 948–960.

Qian, P., Bullough, P.A., and Hunter, C.N. (2008) Three-dimensional reconstruction of a membrane-bending complex. *J Biol Chem* **283:** 14002–14011.

Reilly, P.A., and Niederman, R.A. (1986) Role of apparent membrane growth initiation sites during photosynthetic membrane development in synchronously dividing *Rhodopseudomonas sphaeroides*. *J Bacteriol* **167:** 153–159.

Reynwar, B.J., Illya, G., Harmandaris, V.A., Muller, M.M., Kremer, K., and Deserno, M. (2007) Aggregation and vesiculation of membrane proteins by curvature-mediated interactions. *Nature* **447:** 461–464.

Scheuring, S., Seguin, J., Marco, S., Levy, D., Breyton, C., Robert, B., and Rigaud, J.L. (2003) AFM characterization of tilt and intrinsic flexibility of *Rhodobacter sphaeroides* light harvesting complex 2 (LH2). *J Mol Biol* **325:** 569–580.

Sener, M.K., Olsen, J.D., Hunter, C.N., and Schulten, K. (2007) Atomic level structural and functional model of a bacterial photosynthetic membrane vesicle. *Proc Natl Acad Sci USA* **104:** 15273–15278.

Siebert, C.A., Qian, P., Fotiadis, D., Engel, A., Hunter, C.N., and Bullough, P.A. (2004) Molecular architecture of photosynthetic membranes in *Rhodobacter sphaeroides*: the role of PufX. *EMBO J* **23:** 690–700.

Ting, C.S., Hsieh, C., Sundararaman, S., Mannella, C., and Marko, M. (2007) Cryo-electron tomography reveals the comparative three-dimensional architecture of *Prochlorococcus*, a globally important marine cyanobacterium. *J Bacteriol* **189:** 4485–4493.

Vos, M.H., van Dorssen, R.J., Amesz, J., van Grondelle, R., and Hunter, C.N. (1988) The organisation of the photosynthetic apparatus of *Rhodobacter sphaeroides*: studies of antenna mutants using singlet-singlet quenching. *Biochim Biophys Acta* **933:** 132–140.

Walz, T., Jamieson, S.J., Bowers, C.M., Bullough, P.A., and Hunter, C.N. (1998) Projection structures of three photosynthetic complexes from *Rhodobacter sphaeroides*: LH2 at 6 Å, LH1 and RC-LH1 at 25 Å. *J Mol Biol* **282:** 833–845.

Winkler, H. (2007) 3D reconstruction and processing of volumetric data in cryo-electron tomography. *J Struct Biol* **157:** 126–137.

Worden, P.B., and Sistrom, W.R. (1964) The preparation and properties of bacterial chromatophore fractions. *J Cell Biol* **23:** 135–150.

Zeng, X., Roh, J.H., Callister, S.J., Tavano, C.L., Donohue, T.J., Lipton, M.S., and Kaplan, S. (2007) Proteomic characterization of the *Rhodobacter sphaeroides* 2.4.1 photosynthetic membrane: identification of new proteins. *J Bacteriol* **189:** 7464–7474.

Supporting information

Additional supporting information may be found in the online version of this article.

Please note: Wiley-Blackwell are not responsible for the content or functionality of any supporting materials supplied by the authors. Any queries (other than missing material) should be directed to the corresponding author for the article.